Journal of Quantitative Spectroscopy & Radiative Transfer 329 (2024) 109204

Contents lists available at ScienceDirect

Journal of Quantitative Spectroscopy and Radiative Transfer

journal homepage: www.elsevier.com/locate/jqsrt

# Sensitivity of backscattering to spherical particle physical properties: Size, refractive index, and shape deviations

Prakash Gautam [a,*], Hans Moosmüller [a], Justin B. Maughan [b], Christopher M. Sorensen [c]

[a] Laboratory for Aerosol Science, Spectroscopy, and Optics, Desert Research Institute, Nevada, System of Higher Education, 2215 Raggio Parkway, Reno, NV 89512, USA
[b] Pratt Community College, 348 NE SR 61, Pratt, KS 67124, USA
[c] Department of Physics, Kansas State University, 116 Cardwell Hall, 1228 N. 17th Street, Manhattan, KS 66506, USA

ARTICLE INFO

*Keywords:*
Backscattering
Spherical Particles
Forward scattering
Mie Theory
Lidar Remote Sensing

ABSTRACT

The purpose of this paper is to study the dependency of light backscattering on particle physical properties: size, refractive index, and shape; and to demonstrate the extreme sensitivity of backscattering on these properties. We demonstrate how the nondescript backscattering pattern evolves seemingly chaotic, in contrast to the orderly forward scattering, with the particle's physical properties. The demonstration was carried out by light scattering from water droplets and with spherical particle Mie theory. Our results show systematic, descriptive evolution of the forward scattering pattern, which is clearly shown in logarithmic Q–space, whereas non-descriptive, chaotic evolution within the backscattering regime is displayed in linear θ–space. Additionally, our study shows that within the last 1°, the backscattering intensity remains constant and featureless for the ~ 2.5 μm diameter water droplets investigated here.

## 1. Introduction

Backscattering measurements from the aerosol particles using remote sensing techniques are crucial to gather quantitative information on atmospheric particles' shape, size, and composition from a distance [1]. Such measurements are fundamental to assessing aerosol impacts on climate and global warming, weather patterns, and other meteorological phenomena [2]. Lidar (Light Detection and Ranging) is one of the commonly used active remote sensing techniques collecting backscattered light coming from distant particles [3–5]. Particle properties have been retrieved from the analysis of backscattered light, which is highly sensitive to particle microphysical properties, causing challenges in the assessment and interpretation of collected data. Thus, to retrieve accurate information from backscattering data and radiative transfer calculations, it is imperative to first gain a detailed understand of aerosol backscattering properties [1,2,5,6].

Mie theory [7], an analytical solution to the Maxwell equations for scattering by a homogenous spherical particle, remains the primary approach for calculating the radiative properties of aerosol particles [8]. However, Mie theory-derived optical properties may be significantly different from remote sensing observed properties [1]. In this study, we demonstrate how even a slight change in the microphysical properties of spherical particles can lead to significant changes and poorly described behavior of backscattering properties. This demonstration visualizes scattering data both linearly when plotting them vs. the scattering angle θ and logarithmically when plotting them vs. the magnitude of the scattering wave vector q, called Q–space analysis [9–13]. The core messages conveyed in this paper are straightforward yet significant: 1) to demonstrate the sensitivity of backscattering to changes in particle size and size distribution, refractive index, and shape, 2) to caution against the practice of extrapolating side scattering to that at near and exact backscattering angles, 3) to plot the scattered intensity vs. linear θ, and logarithmic (e.g., Q-space) x-axes to yield a comprehensive description of the whole angular scattering regime.

## 2. Experimental apparatus

The light scattering setup used in this experiment can measure the scattered light intensity over an angular range from 0.32° to 177.6° and corresponding scattering wave vector magnitudes from 660 $cm^{-1}$ to 2.36 × $10^5$ $cm^{-1}$. The light source used for our measurements generates vertically polarized light with a wavelength λ = 532 nm. Water droplets generated with a 6-jet collision nebulizer [14] were used as scattering particles. The laser light interacts with an upward, vertical droplet flow

* Corresponding author.
*E-mail address:* Prakash.Gautam@dri.edu (P. Gautam).

https://doi.org/10.1016/j.jqsrt.2024.109204
Received 1 May 2024; Received in revised form 16 September 2024; Accepted 24 September 2024
Available online 29 September 2024

from an aerosol tube, forming a cylindrically shaped scattering volume. Two multi-channel detectors were used to collect scattered light at 31 angles simultaneously (quasi-simultaneously 46 angles, overall), which allows for a quick and efficient procurement of data. A detailed explanation of the experimental setup and data acquisition methods can be found in [15,16].

## 3. Results

We analyzed our experimentally measured spherical water droplets' light scattering data by plotting versus scattering angle θ, linearly, and as a logarithmic function of the scattering wave vector magnitude q

$$q = 2k\sin(\theta / 2), \tag{1}$$

where $k = 2\pi/\lambda$, with λ being the wavelength. We call plotting scattered intensity, I(q) vs q, on a log-log plot "Q–space analysis" [9,10]. Our measured data were fitted with Mie theory calculations to demonstrate how a small change in particle physical properties affected the scattered intensity, especially in the backscattering regime. The fit accounts for scattering originating from an ensemble of spherical water droplets with a log-normal size distribution. For this, we introduce P(r), which is the unnormalized log-normal size distribution given by

$$P(r) = exp\left(-ln^2\right)\left(\frac{r}{r_0}\right) \Big/ 2ln^2\sigma, \tag{2}$$

where $r_0$, is the most probable radius and σ is the geometric width of the size distribution [17,18]. The fit was carried out in three ways by changing 1) the most probable radius $r_0$, 2) the geometric width of the size distribution σ, and 3) the purely real refractive index m of the water constituting the droplets.

We changed the size distributions in two ways: 1) changing the most probable size by 2.5 % [Fig. 1] and 2) changing the width of the size distribution by the same fractional amount [Fig. 2], while keeping the refractive index constant at m = 1.33. Note that for a change in the most probable size, we kept the width of the particle size distribution constant and vice-versa. Similarly, to understand the evolution of scattering patterns with a change in the real part of the refractive index, we changed m by 2.5 %, while keeping the most probable size $r_0$, and the width of the size distribution σ the same [Fig. 3]. The experimental errors are not shown on the graph because they are too small to be represented.

Figs. 1 and 2 show the fitting of Mie calculations to experimental results for the water droplets, plotted both in conventional θ–space and Q–space. Our data are normalized to 1.0 at the smallest angle or q. Fitting our experimental data over the entire angular range with Mie theory, integrated over the size distribution, yielded the best fit weighted mean radius of $r_0$ = 1.25 μm with a geometric width of $\sigma_0$ = 1.45 for a log-normal distribution. These two values of $r_0$ and $\sigma_0$ are the values at which Mie theory calculations matched best with light scattering data for the entire measured angular scattering range i.e., including all regimes: forward-, side-, and back-scattering, shown in Figs. 1 and 2 (parts a and c, in θ– and Q–space, respectively). A detailed explanation of the three regimes can be found in [19]. In Fig. 1, we have also changed $r_0$ by ± 2.5 %, keeping, $\sigma_0$ and m constant, whereas in Fig. 2, we have also changed $\sigma_0$ by ± 2.5 %, keeping $r_0$ and m constant.

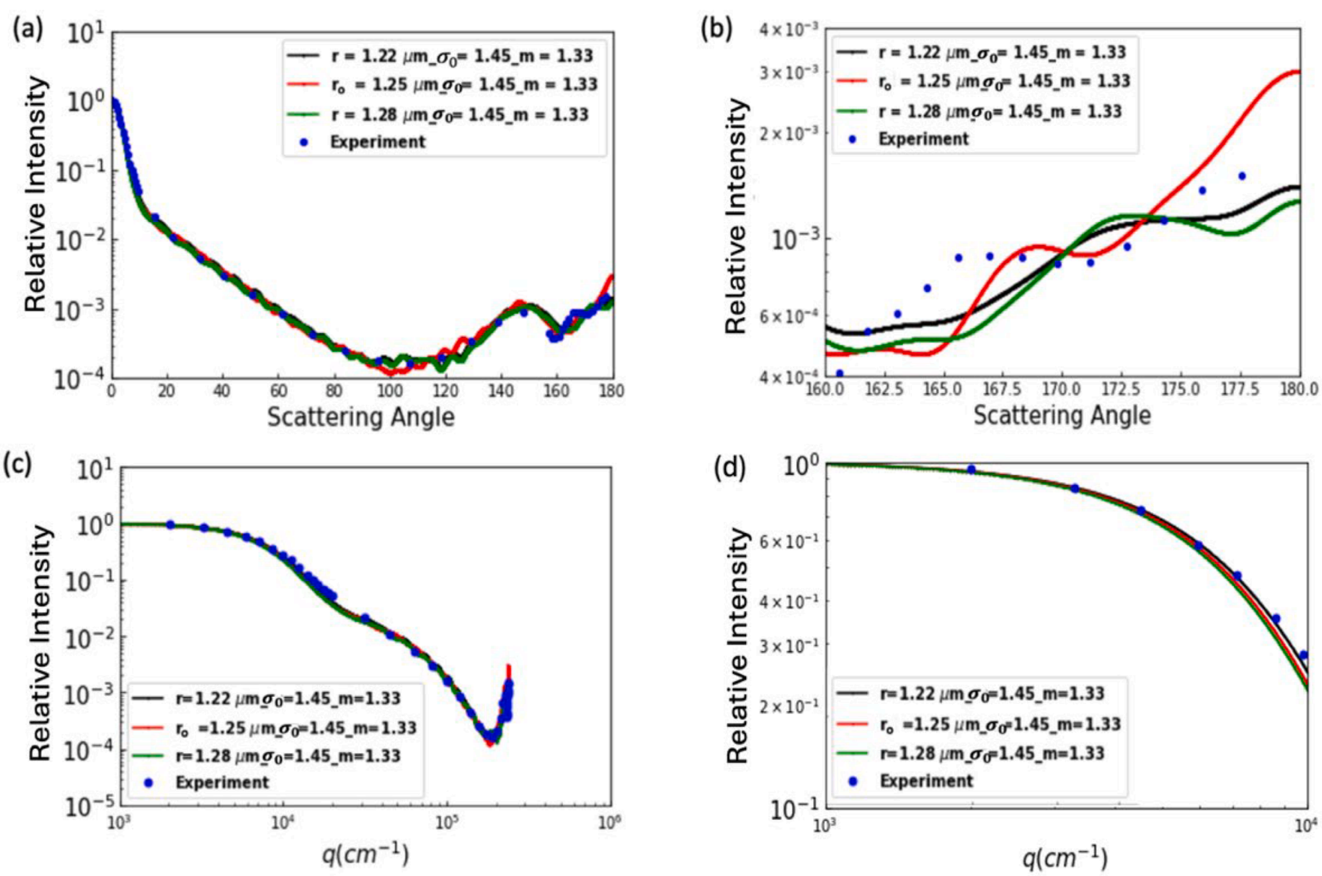


**Fig. 1.** Comparison of the measured forward normalized light scattering data with theoretical Mie calculations. Best fit values are a weighted mean radius of $r_0$ = 1.25 μm with a geometric width of $\sigma_0$ = 1.45 and a refractive index of m = 1.33. In addition, Mie calculations for a ± 2.5 % relative change in the mean radius are displayed. Part (a) is plotted linearly as a function of scattering angle (θ), i.e. θ–space. Part (b) is a magnified graph for the backscattering regime in θ–space. Part (c) plots the same data versus q ($cm^{-1}$) on a log-log scale, i.e., Q–space. Part (d) is a magnified graph for the forward scattering regime in Q–space. The intensity axes of Figs. (b) and (d) are scaled equivalently for comparison.

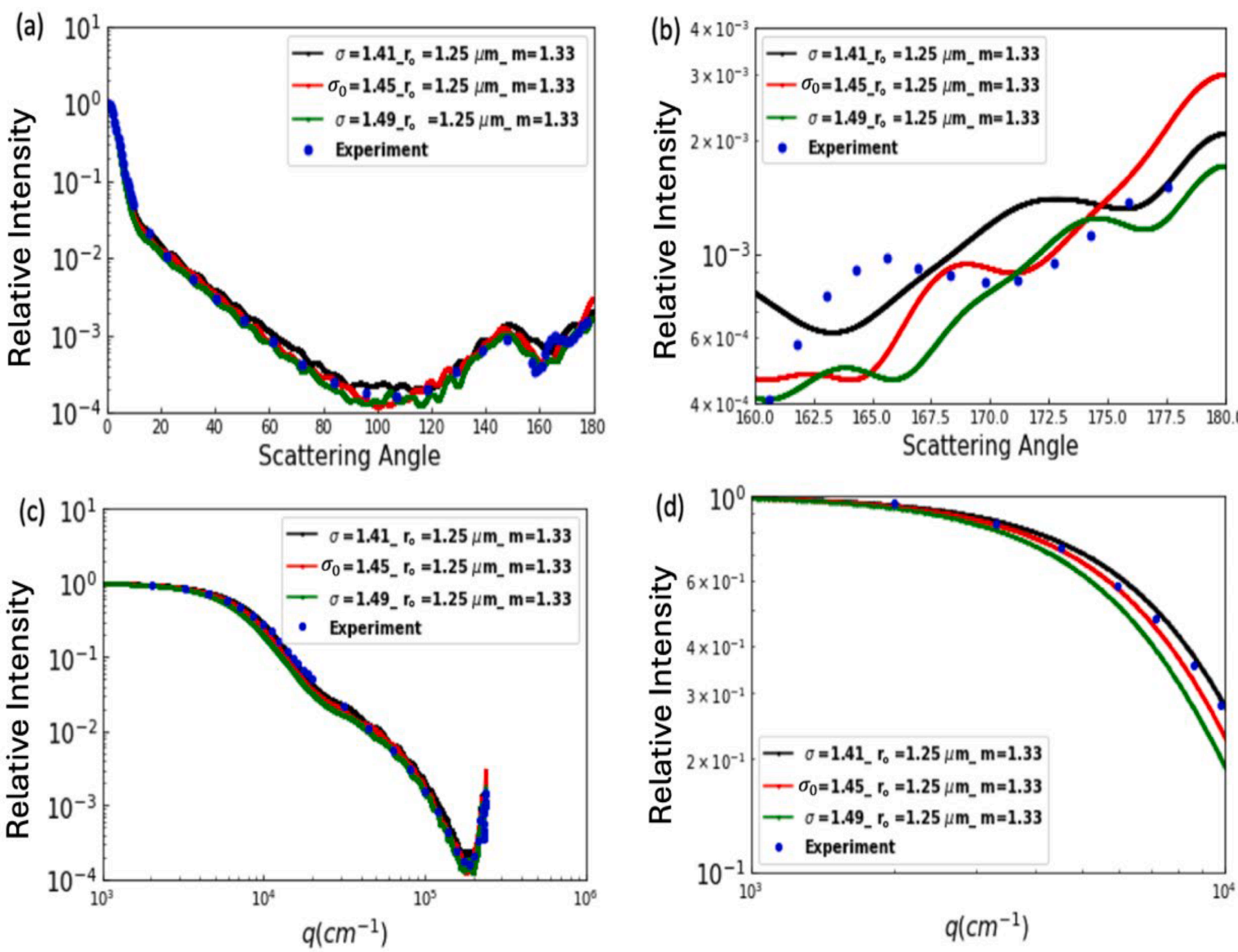


**Fig. 2.** Comparison of the measured forward normalized light scattering data with theoretical Mie calculations. Best fit values are a weighted mean radius of $r_0 = 1.25$ μm with a geometric width of $\sigma_0 = 1.45$ and a refractive index of m = 1.33. In addition, Mie calculations for a ± 2.5 % relative change in the geometric width are displayed. Part (a) is plotted linearly as a function of scattering angle (θ), i.e. θ–space. Part (b) is a magnified graph for the backscattering regime in θ–space. Part (c) plots the same data versus q ($cm^{-1}$) on a log-log scale, i.e., Q–space. Part (d) is a magnified graph for the forward scattering regime in Q–space. The intensity axes of Figs. (b) and (d) are scaled equivalently for comparison.

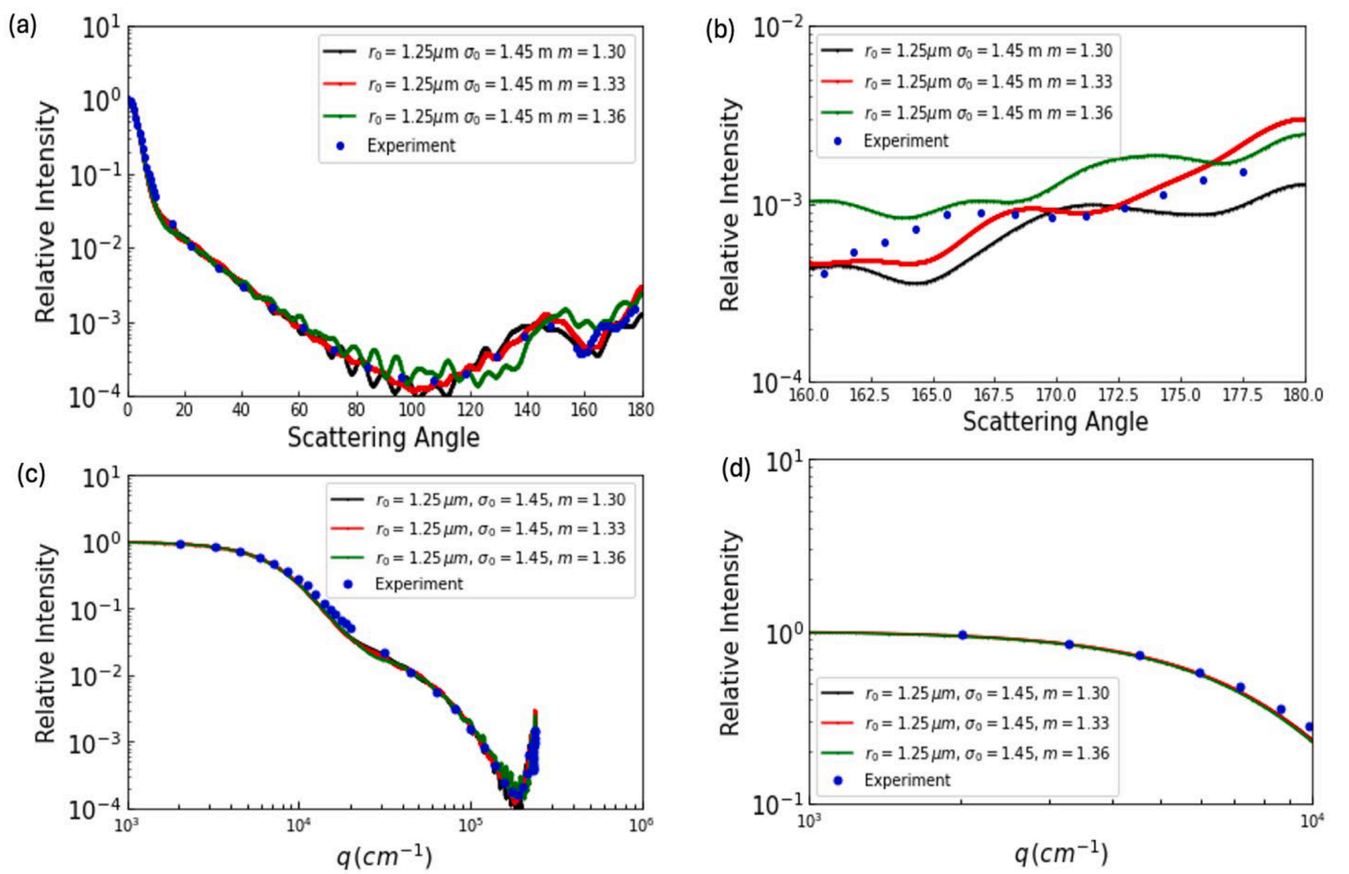


**Fig. 3.** Comparison of the measured forward normalized light scattering data with theoretical Mie calculations. Best fit values are a weighted mean radius of $r_0$ = 1.25 μm with a geometric width of $\sigma_0 = 1.45$ and a refractive index of m = 1.33. In addition, Mie calculations for a ± 2.5 % relative change in the refractive index are displayed. Part (a) is plotted linearly as a function of scattering angle (θ), i.e. θ-space. Part (b) is a magnified graph for the backscattering regime in θ–space. Part (c) plots the same data versus q ($cm^{-1}$) on a log-log scale, i.e. Q–space. Part (d) is a magnified graph for the forward scattering regime in Q–space. The intensity axes of Figs. (b) and (d) are scaled equivalently for comparison.

Through this, our objective is to analyze how the scattering pattern evolves when there is a small change in either the most probable size (Fig. 1 a, c) and geometric width (Fig. 2 a, c) of the size distribution. Focusing on the backscatter regime (160° – 180°), Figs. 1(b) and 2(b) display seemingly chaotic, non-descriptive changes in θ–space, while Figs. 1(d) and 2(d) focus on the forward scattering regime where matched, well-defined forward scattering patterns are obvious in Q–space.

Fig. 3 shows the evolution in the scattering pattern for a small change (± 2.5 %) in the purely real refractive index m while keeping the most probable size $r_0$, and geometric width $\sigma_0$, the same. The angular scattering data over the whole range of scattering angles are shown in Fig. 3 (a) and (c) in θ– and Q–space, respectively. Again, the data were normalized to 1.0 at the smallest scattering angle or q. Our results show that the forward scattering data match well (Fig. 3(d)), with significant differences in the backscattering regime (Fig. 3(b)). Here, the close matching in the forward scattering regime is expected because this regime is diffraction-dominated, and diffraction is fairly insensitive to the shape and refractive index of the particles [10,13]. These results show that backscattering is highly sensitive to particle refractive index, while forward scattering is fairly insensitive to particle refractive index.

To give some practical reality to refractive index changes, we used changes in temperature to induce changes in water's refractive index. With the data provided by [20], we performed Mie calculations for the refractive indices that correspond to the wide range of temperatures 10 °C, 20 °C, 30 °C, 40 °C, and 50 °C. The total angular scattering intensity, both calculated theoretically and measured experimentally, was plotted in both analysis methods: θ–space [Fig. 4a) and Q–space [Fig. 4c]. Figs. 4 (b) and (d) show a non-descriptive, seemingly chaotic scattering pattern at the backscattering regime, compared to the well-described, matched forward scattering regime, respectively. This shows that even a very small temperature related changes in refractive index (i.e., of ∼0.001) causes a noticeable difference in the scattering pattern in the backscattering regime (Fig. 4b).

In a previous study, our group conducted laboratory measurements of light backscattering (180° ± 6°) from well-characterized, micron-sized spherical polystyrene latex (PSL) particles of various sizes [21]. These investigations showed an extreme sensitivity of backscattering to a small change in refractive index and size. Fig. 5 (a) shows the comparisons between experimentally measured backscattering intensity from PSL particles (r = 3.075 μm) with theoretical Mie calculations. The theoretical calculations were carried out for minor refractive index variations around 1.590, the manufacturer's specified refractive index, to optimize the comparisons. The results show that the data were aligned well with the central peak, but deviations were observed at the secondary peak around 176°. Fig. 5 (b) shows the comparison of scattering intensity between an ensemble of spheroid with ε = 1.0 (a sphere), and spheroid with ε = 1.025, mathematically the radius of a spheroid is described by [22]

$$r(\theta) = a\left(\sin^2(\theta) + \frac{a^2}{b^2}\cos^2(\theta)\right) \quad (3)$$

where a is the horizontal semi-axis, and b is the rotational axis semi-axis. The aspect ratio of the spheroid is given by the ratio of the axes $a/b$. A lognormal distribution was used for both ensembles with an average

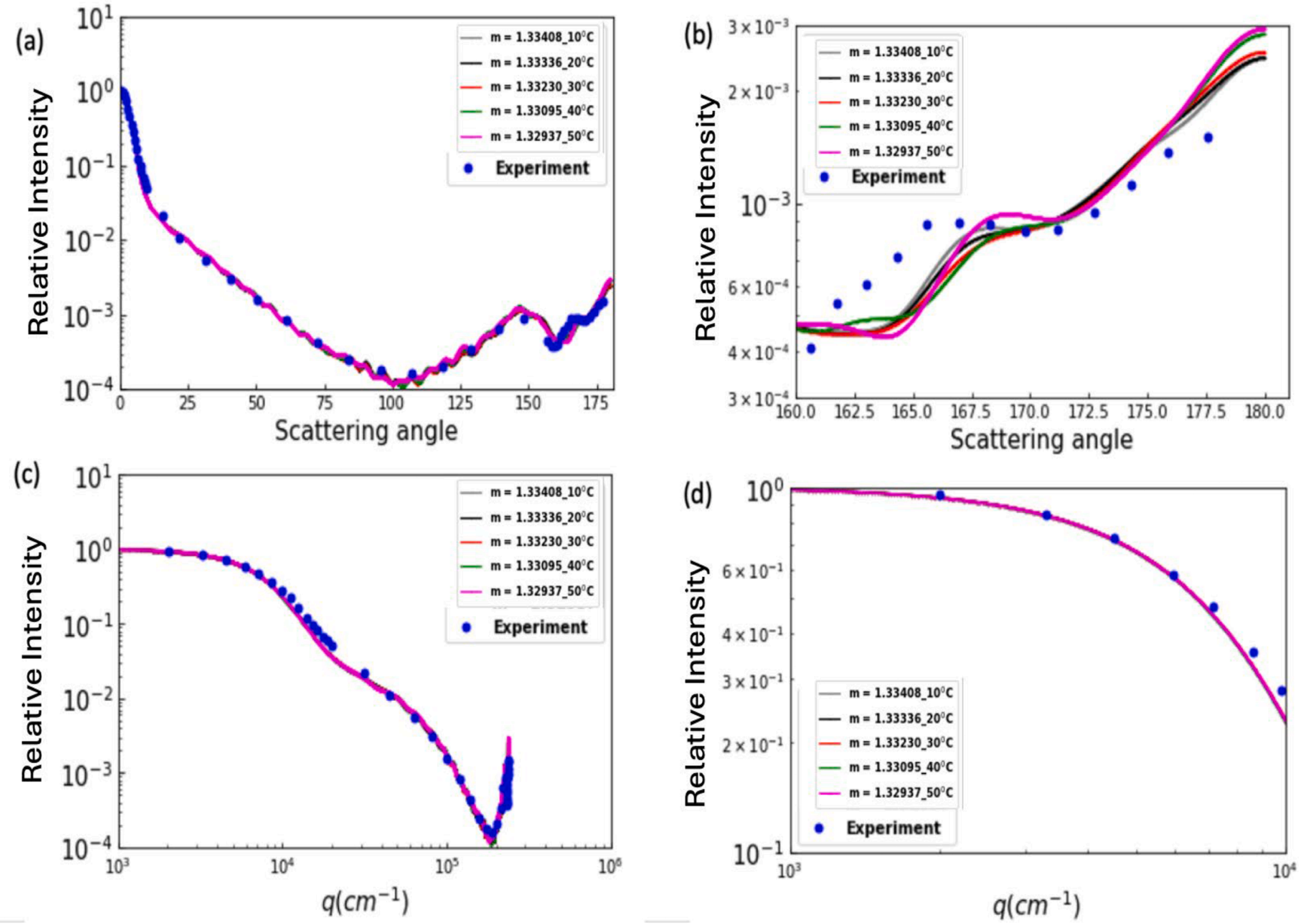


**Fig. 4.** Comparison of the measured forward normalized light scattering data with theoretical Mie calculations. Best fit values are a weighted mean radius of $r_0 = 1.25$ μm with a geometric width of $\sigma_0 = 1.45$ and a refractive index corresponding to different temperatures. Part (a) is plotted linearly as a function of scattering angle (θ), i.e. θ–space. Part (b) is a magnified graph for the backscattering regime in θ–space. Part (c) plots the same data versus q ($cm^{-1}$) on a log-log scale, i.e. Q–space. Part (d) is a magnified graph for the forward scattering regime in Q–space. The intensity axes of Figs. (b) and (d) are scaled equivalently for comparison.

radius of $r = 1.4$ μm and a geometric size distribution width of $\sigma = 1.45$. The calculations were done with the T-Matrix code developed by Mishchenko and Travis [22], the T-Matrix formulation provides an analytical solution for calculations over the shape and both the orientational and size averaging. All setting were kept identical for the spheroids and spheres except the aspect ratio to ensure as much as possible that only the shape was affecting the scattering results. The calculated results show that even an aspect ratio of only 2.5 % away

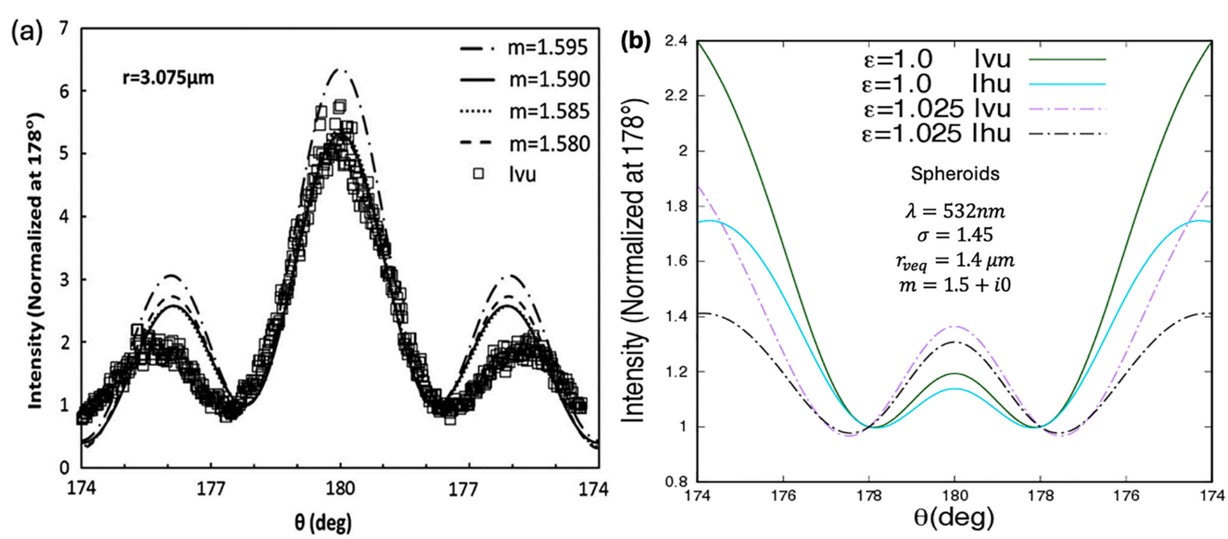


**Fig. 5.** (a) Comparisons of the experimentally measured backscattering intensity normalized at 178° for commercially available polystyrene latex (PSL) spheres with theoretical Mie calculations for vertically polarized light [21] and (b) Demonstration of the effect of shape on backscattering intensity by comparing backscattering intensity from a sphere to that from a spheroid for both vertically and horizontally polarized light.

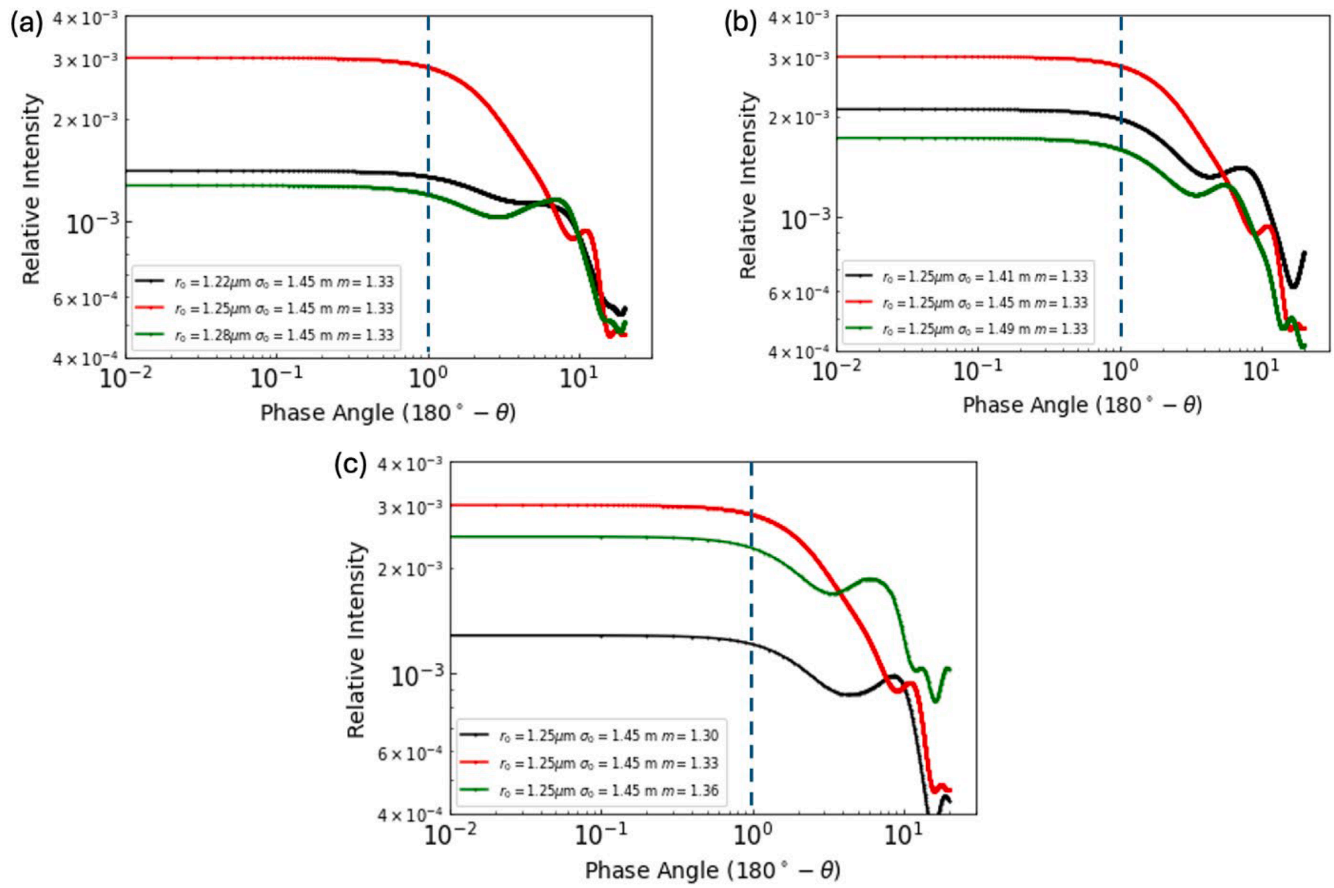


**Fig. 6.** The theoretical Mie calculated backscattering intensity (last ≈ 20 °) plotted as a function of phase angle (180° - θ) on a log-log scale. Part (a) shows the effect of a ± 2.5 % relative change in the weighted mean radius of $r_0 = 1.25$ μm, keeping the geometric width $\sigma_0$, and refractive index m the same. Part (b) shows the effect of a ± 2.5 % relative change in the geometric size distribution of $\sigma_0 = 1.45$, keeping most probable size $r_0$, and refractive index m the same. Part (c) shows the effect of a ± 2.5 % relative change in the refractive index, keeping the most probable size $r_0$ and geometric width $\sigma_0$, the same.

from that of unity. The change in shape significantly affects the angular backscattering intensity, with changes of ~15 % at 180° and up to ~25 % at 174° Overall, a broad range of calculations shows the extreme sensitivity of backscattering to the particle's physical properties: size, refractive index, and shape.

Additionally, to gain a better understanding of scattering evolution at near and exact backscattering (180°) angles, we analyzed Mie scattering calculations using the phase angle (180° - θ) for the last ≈ 20 ° for small changes in most probable size $r_0$, geometric width $\sigma_0$, and refractive indices m. These results are shown in Fig. 6 (a), (b), and (c) respectively. The results show that, for our particle parameters, in the last 1 °, the intensity remains constant and featureless for all cases, but in the limit of phase angle equal zero, significant sensitivity to probable size $r_0$, geometric width $\sigma_0$, and refractive indices m occurs.

## 4. Conclusion

We have demonstrated that for spherical particles, backscattering is strongly dependent on the particle's size, refractive index, and shape deviations. This study emphasizes that while Mie's theory provides accurate light scattering results for spherical particles, interpretation of measured backscattering data requires accurate characterization of particle physical properties, which is complicated by the extreme, seeming chaotic, sensitivity of backscattering to physical particle properties. Overall, the results presented in this work offer practical value to those engaged in particle scattering and to professionals within the lidar and remote sensing communities.

## Authorship contribution statement

All authors reviewed and edited the paper.

## Disclosure statement

No potential conflict of interest was reported by the author(s).


## Funding

Financial support for this work was provided by the National Science Foundation under Grant no. AGM 1649783 and Department of Energy (DOE) Los Alamos National Laboratory (LANL) through Kansas State University (KSU) under Grant no. A23-0465-S001. The work of H.M. was in addition supported in part by NASA grant 80NSSC20M0205 (PACE SAT Project: PACE UV ROAD) and by the National Science Foundation under Grant No. OIA-2148788.


## CRediT authorship contribution statement

**Prakash Gautam:** Writing – review & editing, Writing – original draft, Methodology, Data curation, Conceptualization. **Hans Moosmüller:** Writing – review & editing, Methodology, Conceptualization. **Justin B. Maughan:** Writing – review & editing, Methodology. **Christopher M. Sorensen:** Writing – review & editing, Supervision, Methodology, Conceptualization.

## Declaration of competing interest

The authors declare the following financial interests/personal relationships which may be considered as potential competing interests:

Christopher M Sorensen reports financial support and article publishing charges were provided by National Science Foundation under Grant no. AGM 1,649,783. Christopher M Sorensen reports financial support was provided by Department of Energy (DOE) Los Alamos National Laboratory (LANL) through Kansas State University (KSU) under Grant no. A23–0465-S001. Hans Moosmuller reports financial support was provided by NASA. None If there are other authors, they declare that they have no known competing financial interests or personal relationships that could have appeared to influence the work reported in this paper.

## Data availability

No data was used for the research described in the article.

## References


[1] Ceolato R, Berg MJ. Aerosol light extinction and backscattering: a review with a lidar perspective. J Quant Spectrosc Radiat Transfer 2021;262:107492. https://doi.org/10.1016/j.jqsrt.2020.107492.

[2] Chang Y, Hu Q, Goloub P, Veselovskii I, Podvin T. Retrieval of aerosol microphysical properties from multi-wavelength mie–raman lidar using maximum likelihood estimation: algorithm, performance, and application. Remote Sens 2022; 14:6208. https://doi.org/10.3390/rs14246208.

[3] Satheesh SK, Krishna Moorthy K. Radiative effects of natural aerosols: a review. Atmos Environ 2005;39:2089–110. https://doi.org/10.1016/j.atmosenv.2004.12.029.

[4] Hoff RM, Christopher SA. Remote sensing of particulate pollution from space: have we reached the promised land? J Air Waste Manag Assoc 2009;59:645–75. discussion 642-644.

[5] Tegen I. Modeling the mineral dust aerosol cycle in the climate system. Quat Sci Rev 2003;22:1821–34. https://doi.org/10.1016/S0277-3791(03)00163-X.

[6] Dubovik O, Li Z, Mishchenko MI, Tanré D, Karol Y, Bojkov B, et al. Polarimetric remote sensing of atmospheric aerosols: instruments, methodologies, results, and perspectives. J Quant Spectrosc Radiat Transfer 2019;224:474–511. https://doi.org/10.1016/j.jqsrt.2018.11.024.

[7] Mie G. Beiträge zur Optik trüber Medien, speziell kolloidaler Metallösungen. Ann Phys 1908;330:377–445. https://doi.org/10.1002/andp.19083300302.

[8] Hess M, Koepke P, Schult I. Optical properties of aerosols and clouds: the software package OPAC. Bull Am Meteorol Soc 1998;79:831–44. https://doi.org/10.1175/1520-0477(1998)079<0831:OPOAAC>2.0.CO;2.

[9] Sorensen CM. Q-space analysis of scattering by particles: A review. J Quant Spectrosc Radiat Transfer 2013;131:3–12. https://doi.org/10.1016/j.jqsrt.2012.12.029.

[10] Sorensen CM. Light scattering and absorption by particles: the Q-space approach. IOP Publishing; 2022. https://doi.org/10.1088/978-0-7503-5157-7.

[11] Gautam P, Maughan JB, Sorensen CM. Q-space analysis of experimentally observed light scattering by hematite and molybdenum disulfide particles n.d.

[12] Gautam P, Maughan JB, Ilavsky J, Sorensen CM. Light scattering study of highly absorptive, non-fractal, hematite aggregates. J Quant Spectrosc Radiat Transfer 2020;246:106919. https://doi.org/10.1016/j.jqsrt.2020.106919.

[13] Gautam P, Sorensen CM. A light-scattering study of highly refractive, irregularly shaped MoS2 particles. J Quant Spectrosc Radiat Transfer 2020;242:106757. https://doi.org/10.1016/j.jqsrt.2019.106757.

[14] May KR. The collison nebulizer: description, performance and application. J Aerosol Sci 1973;4:235–43. https://doi.org/10.1016/0021-8502(73)90006-2.

[15] Gautam P, Sorensen CM. A wide range (0.32°–177.6°), multi-angle light scattering setup and concomitant analysis method. Rev Sci Instrum 2021;92:113105. https://doi.org/10.1063/5.0068318.

[16] Light Scattering Study of Irregular Particles with Arbitrary Size, Shape, and Complex Refractive Index (PhD Thesis). Kansas State University. https://krex.k-state.edu/handle/2097/42344.

[17] Sorensen CM. Light scattering by fractal aggregates: a review. Aerosol Sci Technol 2001;35:648–87. https://doi.org/10.1080/02786820117868.

[18] Heinson YW. Light scattering studies of irregularly shaped particles (PhD Thesis). 2016.

[19] Gautam P, Moosmüller H, Maughan JB, Sorensen CM. Light scattering from spherical and irregular particles over a wide angular range. Aerosol Sci Technol 2024:1–10. https://doi.org/10.1080/02786826.2024.2338543.

[20] Bashkatov AN, Genina EA. Water refractive index in dependence on temperature and wavelength: a simple approximation. Saratov Fall Meeting 2002: Optical Technol Biophy Med IV 2003;5068:393–5. https://doi.org/10.1117/12.518857. SPIE.

[21] Heffernan BM, Heinson YW, Maughan JB, Chakrabarti A, Sorensen CM. Backscattering measurements of micron-sized spherical particles. Appl Opt 2016; 55:3214–8. https://doi.org/10.1364/AO.55.003214. AO.

[22] Mishchenko MI, Travis LD. Capabilities and limitations of a current FORTRAN implementation of the *T*-matrix method for randomly oriented, rotationally symmetric scatterers. J Quant Spectrosc Radiat Transfer 1998;60:309–24. https://doi.org/10.1016/S0022-4073(98)00008-9.